# Geometrical scaling law for laser-induced micro-projectile impact testing

Z.P. Gu [a,b,1], Y.J. Cheng [a,b,1], K.L. Xiao [a], K. Li [b,d], X.Q. Wu [a,b,*], Q.M. Li [c], C.G. Huang [b,e]

[a] *Key Laboratory of Mechanics in Fluid Solid Coupling Systems, Institute of Mechanics, Chinese Academy of Sciences, Beijing 100190, China*
[b] *School of Engineering Science, University of Chinese Academy of Sciences, Beijing 100049, China*
[c] *Department of Mechanical, Aerospace and Civil Engineering, School of Engineering, The University of Manchester, Manchester M13 9PL, UK*
[d] *National Microgravity Laboratory, Institute of Mechanics, Chinese Academy of Sciences, Beijing 100190, China*
[e] *Hefei Institutes of Physical Science, Chinese Academy of Sciences, Heifei 230031, China*

A B S T R A C T

Laser-induced micro-projectile impact testing (LIPIT) is a useful experimental method for exploring the dynamic behavior of materials at microscale. It has been a key issue to obtain a scaling law of launch velocity of LIPIT to simplify experimental design and improve experimental configuration. This paper obtains a geometrical scaling law of launch velocity for LIPIT with relative thick metallic film (30–80 μm thick aluminum) using dimensional analysis, experimental measurements, and numerical simulations. Firstly, the dimensional analyses of LIPIT with and without elastomer film configuration are performed, and the dimensionless parameters controlling the launch velocity of the micro-projectile are deduced, from which the geometrical scaling laws of launch velocity for the LIPIT are obtained. Then, the numerical simulation models of the LIPIT are established and validated by LIPIT experimental results, providing a numerical validation for the geometrical scaling laws. In addition, the influences of the dimensionless parameters on the dimensionless launch velocity of micro-projectiles are analyzed by numerical simulations, and the dimensionless formulas for predicting the launch velocities of micro-projectiles in a LIPIT are given, providing an effective method for analyzing and optimizing the LIPIT experiments.

## 1. Introduction

Understanding the dynamic mechanical behavior of materials subjected to high-velocity impact is a key issue for designing high-performance protective structures [1–3]. The traditional dynamic techniques at macroscale include fatigue testing machine, pendulum impact, drop hammer impact, split Hopkinson pressure bars, Taylor impact, ballistic impact, and plate impact for various application backgrounds and strain rates [4–14]. Although relative large-scale testing is important for understanding material and structural responses, it has been shown that surprising material behavior can emerge with decreasing size scales and increasing strain rates [14–16]. For instance, two-dimensional materials such as graphene are founded to possess excellent mechanical behavior and superior impact resistance [2,17,18]. The traditional impact facilities, such as ballistic impact [12], are incapable of measuring the impact resistance of materials with a thickness in the order of nano- or micro-meters. It is, therefore, crucial to

develop micro-scale impact experimental methods to investigate the dynamical performance of materials at nano- and micro-scales [19–21].

Laser-induced micro-projectile impact testing (LIPIT) has recently attracted great attention due to its capability of exploring the dynamic behavior of materials at microscale. It was firstly developed by Lee et al. [2,22] and further developed by Veysset et al. [23]. The LIPIT utilizes laser-induced shock waves to accelerate micro-projectiles. Generally, the configuration and the launch principle of a LIPIT are shown in Fig. 1 (a) [22–28]. A thin metallic film is attached firmly to a transparent optical glass, and a thin layer of elastomer spreads evenly on the rear surface of the metallic thin film [24]. A micro-projectile is then placed on the back free surface of the elastomer before experiments. When a high power density laser irradiates the surface of a metallic film attached to the optical glass, a thin layer of the metallic film is vaporized and ionized immediately, generating plasma with high pressure during rapid expansion under the confinement of surrounding materials and resulting in a shock pressure with a high amplitude of several GPa and a short duration of tens of nanoseconds [29–31]. The shock wave propagates

---

**Nomenclature**

| | |
|---|---|
| $S_L$ | spot area of laser |
| $E_L$ | energy of laser |
| $t_L$ | full width at half maximum (FWHM) of laser |
| $t_0$ | FWHM of $p(t)$ |
| $t$ | time |
| $S_0$ | effective loading area |
| $p(t)$ | shock wave of plasma generated from laser |
| $p(\tau)$ | pressure of plasma at the time $\tau$ when the laser is switched off |
| $p_0$ | peak pressure of $p(t)$ |
| $I(t)$ | absorbed laser power density |
| $L(t)$ | thickness of the plasma |
| $L(\tau)$ | thickness of the plasma at time $\tau$ |
| $\gamma$ | thermal to internal energy ratio |
| $A$ | yield stress |
| $B$ | strain-hardening modulus |
| $C$ | strain-rate hardening parameter |
| $\overline{\varepsilon^p}$ | equivalent plastic strain |
| $\dot{\varepsilon}^*$ | normalized equivalent plastic strain rate |
| $C_0$ | intercept of the shock velocity-particle velocity curve |

| | |
|---|---|
| $S_1, S_2, S_3$ | slope coefficients of the shock velocity-particle velocity curve |
| $\rho$ | current density |
| $\rho_0$ | initial density |
| $E$ | initial internal energy |
| $\rho_m$ | density of metallic film |
| $E_m$ | elastic modulus of metallic film |
| $\nu_m$ | Poisson's ratio of metallic film |
| $A_m$ | yield stress of metallic film |
| $B_m$ | strain-hardening modulus of metallic film |
| $n_m$ | strain-hardening exponent of metallic film |
| $C_m$ | strain-rate hardening parameter of metallic film |
| $C_{m0}$ | sound speed at zero pressure of metallic film |
| $h_m$ | thickness of metallic film |
| $\rho_e$ | density of elastomer |
| $E_e$ | characteristic elastic modulus of elastomer |
| $\nu_e$ | Poisson's ratio of elastomer |
| $h_e$ | thickness of elastomer |
| $M_p$ | mass of micro-projectile |
| $\nu_p$ | launch velocity of the micro-projectile |
| $\nu_{P-E}$ | experimental launch velocity of the micro-projectile |

back and forth in the thin metallic film and the thin elastomer, leading to the rapid expansion of the thin metallic film and the thin elastomer [32]. As a result, the micro-projectile is finally ejected due to the expansion processes of the thin films, similar to the mechanism of the laser-driven flyer [33,34]. The elastomer film in LIPIT is used to attenuate the shock wave and protect the micro-projectile from laser-induced ablation. Sometimes, the LIPIT configuration without elastomer is employed to increase the launch velocity of the micro-projectile [23].

The configuration of the launchpad is important for LIPIT to realize different launch conditions. For LIPIT with elastomer film, the thickness of the metallic film is in the order of nanometers ($50 \sim 100$ nm), and the thickness of elastomer film is in the order of tens of microns ($20 \sim 50$ μm). The metallic film could be fully ablated under laser irradiation, and only the elastomer film is accelerated by the expanding plasma. With this method, the micro-projectile with a diameter of $5 \sim 30$ μm can be eventually launched at a velocity up to $10^3$ m/s [16,18,35–38]. To further increase the launch velocity, Veysset *et al.* improve the configuration of LIPIT and realize a launch velocity of 3000 m/s for silica micro-projectiles with a diameter of 7.4 μm by removing the elastomer film and increasing the thickness of the metallic film (gold, 670 nm thick) [23]. Sometimes relatively large micro-projectiles ($50 \sim 400$ μm diameter) are required, and relatively thick metallic films ($30 \sim 80$ μm) are used [26], in which the metallic is not fully consumed and expanded with elastomer. In this study, we mainly focus on the scaling law of the launchpad configuration with micron-thick metallic films ($30 \sim 80$ μm). The other launchpads of LIPIT can be investigated with the same method.

LIPIT is currently limited in the launch velocities of micro-projectiles, which prohibits the study of certain impact regimes in certain materials. Here, we will figure out the launch mechanism of LIPIT with relatively thick metallic film and determine the influencing factors of launch velocities of micro-projectiles, so that the configuration of the LIPIT can be improved to achieve even high launch velocity. The launch velocities of micro-projectiles in LIPIT are affected by various parameters involving laser power density and laser spot diameter, geometrical dimensions and mechanical behavior of thin metallic film and thin elastomer, and the type of micro-projectiles. The influence of some individual parameters such as laser pulse energy, micro-projectile mass, and type of elastomer films has been investigated [2,23]. However, essential dimensionless parameters of LIPIT that determine the

launch velocities of micro-projectiles have not been derived. In this paper, the geometrical scaling laws for LIPIT with and without elastomer film configurations are obtained and validated by dimensional analysis and numerical simulation, respectively. In addition, the influence of each essential dimensionless parameter is analyzed numerically, from which specific dimensionless formulas are obtained to predict accurately the launch velocities of micro-projectiles in LIPIT for various experimental configurations.

This paper is organized as follows. In Section 2, the geometrical scaling law of launch velocity for LIPIT is deduced. In Section 3, LIPIT experimental details are provided. In Section 4, numerical simulation models are built. In Section 5, the effects of the dimensionless parameters of the scaling law are analyzed, and the specific formulas used to predict the launch velocity of the micro-projectiles are given, followed by discussion and conclusions.

## 2. Dimensional analysis

In this section, the dimensional analysis is performed to derive the key dimensionless parameters that control the launch velocity of the micro-projectile, from which a geometrical scaling law is obtained.

In LIPIT experiments, the laser pulse with a spot area $S_L$, energy $E_L$, and a full width at half maximum (FWHM) of duration $t_L$ will generate a shock wave $p(t)$ with peak pressure $p_0$ and FWHM $t_0$, which depends on the absorbed laser power density $I(t)$,

$$I(t) = p(t)\frac{dL(t)}{dt} + \frac{3}{2\gamma}\frac{d[P(t) \times L(t)]}{dt}, \tag{1}$$

where $L(t)$ is thickness of plasma; $\gamma$ is thermal internal energy ratio, which is 0.1 for the LIPIT model [29]. When the laser is switched off, the plasma expands adiabatically and its thickness can be determined as

$$p(t) = p(\tau)\left(\frac{L(\tau)}{L(t)}\right)^\delta, \tag{2}$$

where $\delta$ is the adiabatic exponent and typically taken as 2.0, and $p(\tau)$ and $L(\tau)$ are the pressure and thickness of the plasma at the time when the laser is switched off, respectively [29]. The strength-to-pressure ratio of the confined layer and the absorption layer are usually larger than $6 \times 10^{-2}$ under laser-induced shock. As a result, the strength of the
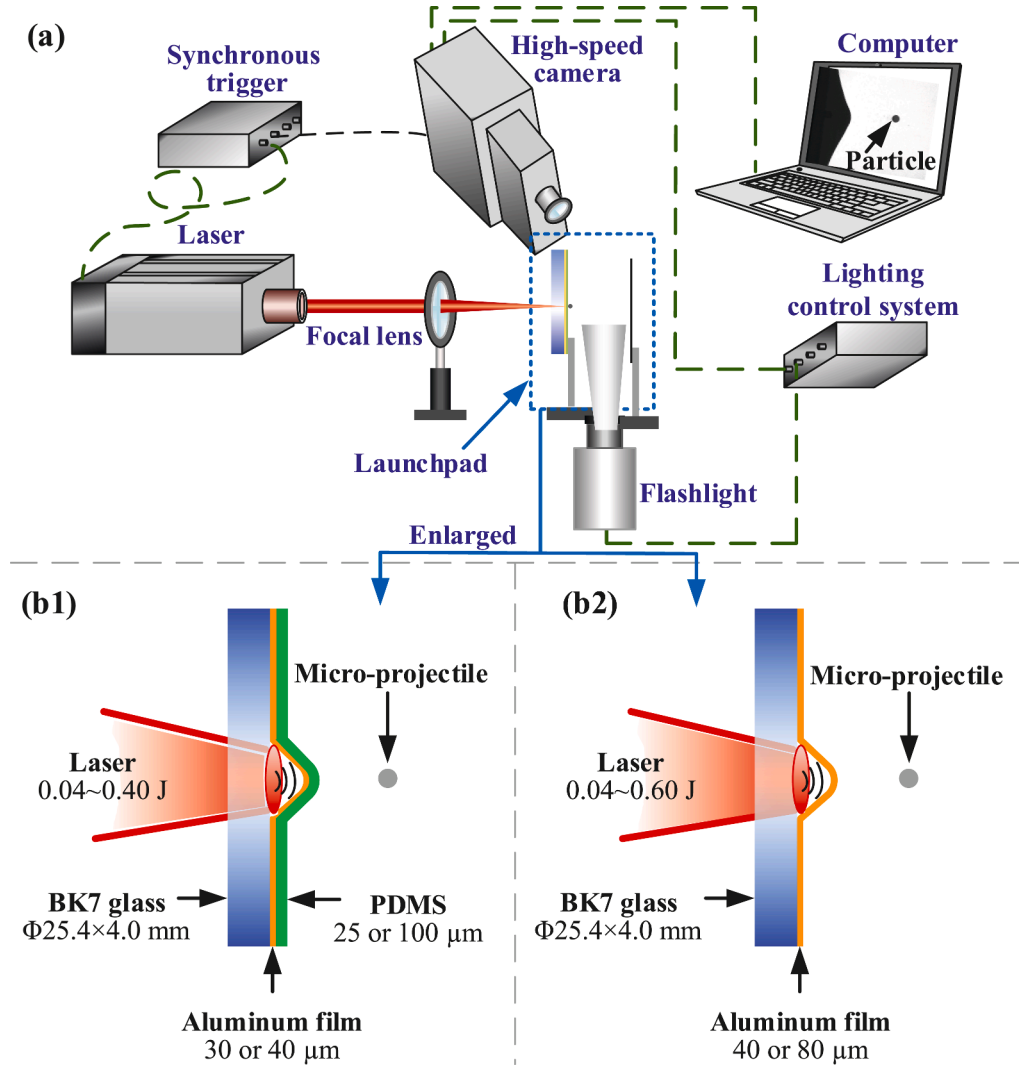
**Fig. 1.** (a) Schematic of the LIPIT system and the launch mechanism (b1) with PDMS and (b2) without PDMS film. The high-intensity laser irradiates the surface of a metallic film to generate plasma with high pressure. During the fast expansion of the plasma, the micro-projectile that is initially attached to the PDMS or the aluminum film is ejected [24], realizing the supersonic impact response of materials under ultra-high strain rates.

material needs to be taken into account. In addition, the reflection of stress waves in the thin aluminum film will affect the expanding velocity of the laser-induced plasma, which should be considered in the present study. Therefore, the coupling effects between the evolution of plasma and the dynamic response of the confined materials are considered and described as follows,

$$\frac{dL(t)}{dt} = f\left(p(t), \frac{dp(t)}{dt}, H_m, \varphi_m\right), \tag{3}$$

where $H_m$ represent thicknesses of confined layer and absorption film, and $\phi_m$ are material constitutive related parameters. The pressure history can be calculated by Eqs. (1)–(3) step by step using a differential computation code [39].

Generally, the duration of shock pressure is about tens of nanoseconds [40]; the micro-projectile launch process is in the order of several microseconds; and the depth of the thermal influence of the laser on the metallic film is about 0.1 μm [41]. Therefore, the present study can analyze separately the laser-matter interaction and micro-projectile launch process for a 10-μm-thick metallic film [42]. Here, for the sake of simplicity, the characteristics of the shock wave, i.e. peak pressure $p_0$, effective area $S_0$, and characteristic duration $t_0$, which can be calculated from Eqs. (1)–(3) for a given laser, are taken into account as input

quantities in the dimensional analysis. As a result, the thermal-related parameters during laser-matter interaction are not taken into account.

The mechanical behavior of the metallic film under shock pressure can be described by the hydro-elastoplastic model [39], in which the relationship between the effective stress and the equivalent plastic strain is given as follows,

$$\sigma_y = (A + B\overline{\varepsilon^p}^n)(1 + C\ln\dot{\varepsilon}^*), \tag{4}$$

where $A$, $B$, $C$, $\overline{\varepsilon^p}$, $n$, and $\dot{\varepsilon}^*$ are yield stress, strain-hardening modulus, strain-rate hardening parameter, equivalent plastic strain, strain-hardening exponent, and the normalized equivalent plastic strain rate [43], respectively. In the present study, the influence of the thermal softening effect of the metallic film on the launch velocity is negligible, it is not considered to increase the computational efficiency (see Appendix). The Mie-Grüneisen equation of state (EOS) [44] with cubic shock velocity-particle velocity is adopted to describe the bulk compressive behavior of the metallic film, in which the pressure is defined as

$$P = \frac{\rho_0 C_0^2 \mu_0 \left[1 + \left(1 - \frac{\gamma_0}{2}\mu_0\right) - \frac{a}{2}\mu_0^2\right]}{\left[1 - (S_1 - 1)\mu_0 - S_2\frac{\mu_0^2}{\mu_0+1} - S_3\frac{\mu_0^3}{(\mu_0+1)^2}\right]^2} + (\gamma_0 + a\mu_0)E, \tag{5}$$

where $\mu_0 = \rho/\rho_0 - 1$, $C_0$ denotes intercept of the shock velocity-particle

velocity curve, $S_1, S_2, S_3$ are slope coefficients of the shock velocity-particle velocity curve, $\gamma_0$ is Grüneisen constant, $a$ denotes first order volume correction to $\gamma_0$, $\rho$ and $\rho_0$ are current density and initial density, $E$ is initial internal energy [44], respectively. The mechanical behavior of the elastomer film covering the metallic film is regarded as super-elastic under impact [45,46], which can be described by the

Ogden Rubber constitutive model,

$$W = \sum_{i=1}^{3} \sum_{j=1}^{n} \frac{\mu_j}{\alpha_j} (\lambda_i{}^{\alpha_j} - 1) + K(J - 1 - lnJ), \tag{6}$$

where $W$ is strain energy density, $\mu_j$ is jth shear modulus, $\alpha_j$ is the jth exponent, $K$ is bulk modulus, $J$ is relative volume; $\lambda_i$ are principal stretches, $n$ is order of the Ogden model [46].

Here, the deformation of micro-projectiles during launching in LIPIT is not considered, and it is therefore regarded as a rigid body. The micro-projectiles might experience large deformation and fracture for ultra-high shock pressure conditions. However, to measure the impact resistance of thin films, the micro-projectiles are generally acted as rigid in experiments to ensure sufficient measurement accuracy. The justification of the rigid assumption of the micro-projectiles is provided in Section Appendix.

According to Buckingham's Π theorem [47], a physical process can be described by a dependent variable, $a_0$, and $n$ independent variables, $a_1, a_2, a_3, \ldots, a_n$, as follows,

$$a_0 = f(a_1, a_2, a_3, \ldots a_n), \tag{7}$$

where $f$ is the function of the physical process [48]. If the number of fundamental quantities is $m$, e.g. $a_1, a_2, a_3, \ldots, a_m$, then Eq. (7) can be written as [29]

$$\frac{a_0}{a_1^{b_1} a_2^{b_2} \ldots a_m^{b_m}} = f\left(\overbrace{1, 1, \ldots, 1}^{m}; \frac{a_{m+1}}{a_1^{p_1} a_2^{p_2} \ldots a_m^{p_m}}, \frac{a_{m+2}}{a_1^{q_1} a_2^{q_2} \ldots a_m^{q_m}}, \ldots, \frac{a_n}{a_1^{r_1} a_2^{r_2} \ldots a_m^{r_m}}\right) \tag{8}$$

The left side of Eq. (8) is dimensionless dependent variable denoted as Π. On the right of Eq. (8), the first $m$ independent variables equal 1, which do not influence the dimensionless dependent variable Π. Therefore, the dimensionless dependent variable Π is influenced by the rest $n$-$m$ independent variables denoted as $\Pi_1, \Pi_2, \cdots, \Pi_{n-m}$, where $\Pi_1 = \frac{a_{m+1}}{a_1^{p_1} a_2^{p_2} \ldots a_m^{p_m}}$, $\Pi_2 = \frac{a_{m+2}}{a_1^{q_1} a_2^{q_2} \ldots a_m^{q_m}}$, $\ldots, \Pi_{n-m} = \frac{a_n}{a_1^{r_1} a_2^{r_2} \ldots a_m^{r_m}}$, and $p_1, \cdots, p_m, q_1, \cdots, q_m, r_1, \cdots, r_m$ are power exponents.

In the present study, the parameters controlling the launch velocity of the LIPIT process are described as follows. The laser shock pressure-related parameters: peak pressure $p_0$, effective loading area $S_0$, and the characteristic duration $t_0$. The mechanical and geometrical parameters of the metallic film include density $\rho_m$, elastic modulus $E_m$, Poisson's ratio $\nu_m$, yield stress $A_m$, strain-hardening modulus $B_m$, strain-hardening exponent $n_m$, strain-rate hardening parameter $C_m$, sound speed at zero pressure $C_{m0}$, dimensionless quantities $S_{m1}, S_{m2}, S_{m3}, \gamma_m, a_m$, and thickness $h_m$. The mechanical and geometrical parameters of the thin elastomer are density $\rho_e$, characteristic elastic modulus $E_e$, Poisson's ratio $\nu_e$, and thickness $h_e$. Since the micro-projectile is assumed as rigid and its dimension is generally a small quantity when compared to the effective

laser loading area, only the mass $M_p$ is considered. The influence of the micro-projectile's diameter is also investigated in Section Appendix, indicating the effect of micro-projectile size is negligible in the present diameter range. As a result, the launch velocity of the micro-projectile, $\nu_p$, can be expressed as

$$\nu_p = f\left(p_0, S_0, t_0; \rho_m, E_m, \nu_m, h_m, A_m, B_m, n_m, C_m, C_{m0}, S_{m1}, S_{m2}, S_{m3}, \gamma_m, a_m; \rho_e, E_e, \nu_e, h_e; M_p\right), \tag{9}$$

where, $p_0, S_0, t_0$ are parameters of laser; $\rho_m, E_m, \nu_m, h_m, A_m, B_m, n_m, C_m, C_{m0}, S_{m1}, S_{m2}, S_{m3}, \gamma_m, a_m$ are parameters of metallic film; $\rho_e, E_e, \nu_e, h_e$ are parameters of elastomer film; and $M_p$ is the parameter of micro-projectile.

Taking $p_0$, $S_0$, and $t_0$ as independent variables, according to the Π theorem [47], Eq. (9) can be rewritten as

where $\Pi_\nu = \nu_p M_p / p_0 S_0 t_0$, $\Pi_p = \rho_m (C_{m0})^2 / p_0$, $\Pi_{E_m} = E_m / p_0$, $\Pi_S = h_m / S_0^{0.5}$,

$$\Pi_\nu = f\left(\nu_m, n_m, C_m, S_{m1}, S_{m2}, S_{m3}, \gamma_m, a_m, \Pi_p, \Pi_{E_m}, \Pi_S, \Pi_{A_m}, \Pi_{B_m}, \Pi_I; \nu_e, \Pi_\rho, \Pi_{E_e}, \Pi_h; \Pi_{M_e}\right), \tag{10}$$

$\Pi_{A_m} = A_m / E_m$, $\Pi_{B_m} = B_m / E_m$, $\Pi_I = C_{m0} \rho_m h_m / p_0 t_0$, $\Pi_\rho = \rho_e / \rho_m$, $\Pi_{E_e} = E_e / E_m$, $\Pi_h = h_e / h_m$, $\Pi_{M_e} = M_p / \rho_e h_e S_0$. $\Pi_\nu$ represents the ratio of micro-projectile momentum to momentum of shock wave. Therefore, nineteen dimensionless parameters affect the dimensionless launch velocity $\Pi_\nu$:

- Poisson's ratios, $\nu_m$ and $\nu_e$, of the metallic film and thin elastomer, respectively.
- Dimensionless EOS related parameters, $n_m, C_m, S_{m1}, S_{m2}, S_{m3}, \gamma_m$, and $a_m$, of the thin metallic film.
- Characteristic pressures, $\Pi_p$ and $\Pi_{E_m}$ representing the deformation mechanism of the thin metallic film.
- Characteristic strain, $\Pi_{A_m}$, and characteristic modulus, $\Pi_{B_m}$, representing the maximum elastic strain and the strain-hardening behavior of the metallic film, respectively.
- Characteristic thickness, $\Pi_S$, of the thin metallic film, representing the stress-state of the shock wave.
- Characteristic momentum, $\Pi_I$, representing the effective loading efficiency of the shock wave.
- Characteristic density, $\Pi_\rho$, and characteristic elastic modulus, $\Pi_{E_e}$, characteristic thickness, $\Pi_h$, of the thin elastomer, respectively.
- Characteristic mass, $\Pi_{M_e}$, of the micro-projectile, representing the inertial effect.

The material-related dimensionless parameters in the bracket on the right-hand side in Eq. (10) remain constant if the metallic film and the elastomer materials are unchanged. Therefore, a simpler relationship is achieved as follows,

$$\Pi_\nu = f\left(\Pi_p, \ \Pi_S, \ \Pi_I, \ \Pi_h, \Pi_{M_e}\right). \tag{11}$$

For the case without the elastomer configuration, as shown in Fig. 1 (b2), the elastomer related parameters will not be considered, and Eq. (10) can be written as

$$\Pi_\nu = g\left(\nu_m, n_m, C_m, S_{m1}, S_{m2}, S_{m3}, \gamma_m, a_m, \Pi_p, \Pi_{E_m}, \Pi_S, \Pi_{A_m}, \Pi_{B_m}, \Pi_I; \Pi_{M_m}\right), \tag{12}$$

where $\Pi_{M_m} = M_p / \rho_m h_m S_0$. Similarly, the following relationship can be obtained if the material of the metallic thin film is unchanged,

**Table 1**

Experimental parameters of the LIPIT.

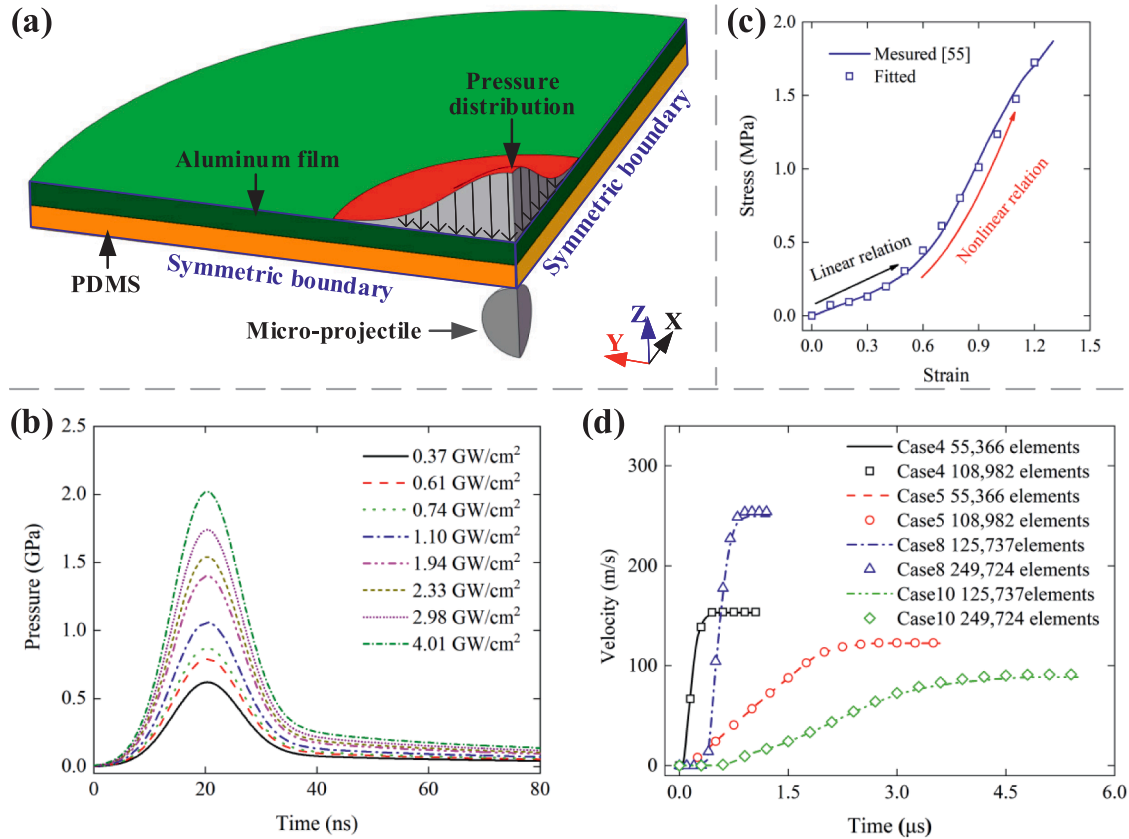| CaseNo. | $E_L$(J) | $R$(mm) | $E_{Ld}$(GW/cm$^2$) | $p_0$(GPa) | $h_{Al}$(μm) | $h_{PDMS}$(μm) | $M_P$(μg) | $v_{P-E}$(m/s) |
|---|---|---|---|---|---|---|---|---|
| 1 | 0.064 | 0.4 | 2.33 | 1.54 | 40 | \ | 0.0113 | 364 ± 6 |
| 2 | 0.063 | 0.3 | 4.08 | 2.04 | 40 | \ | 0.0113 | 473 ± 9 |
| 3 | 0.046 | 0.3 | 2.98 | 1.74 | 40 | \ | 0.173 | 331 ± 5 |
| 4 | 0.016 | 0.5 | 0.37 | 0.62 | 40 | \ | 1.388 | 129 ± 4 |
| 5 | 0.554 | 1.7 | 1.12 | 1.07 | 80 | \ | 175.8 | 118 ± 5 |
| 6 | 0.108 | 0.4 | 3.94 | 2.0 | 30 | 25 | 0.173 | 511 ± 10 |
| 7 | 0.046 | 0.5 | 1.07 | 1.05 | 40 | 100 | 1.388 | 157 ± 3 |
| 8 | 0.083 | 0.5 | 1.94 | 1.4 | 40 | 100 | 1.388 | 234 ± 5 |
| 9 | 0.302 | 1.7 | 0.61 | 0.79 | 40 | 100 | 175.8 | 73 ± 3 |
| 10 | 0.366 | 1.7 | 0.74 | 0.87 | 40 | 100 | 175.8 | 81 ± 3 |



**Fig. 2.** Numerical simulation model of LIPIT. (a) Schematic of the numerical models. A 1/4 model is built due to the symmetries of the geometry and the pressure distribution. The shock pressure is applied on the top surface of the aluminum film. (b) Shock pressure histories on the aluminum film. Various shock pressure profiles at different laser power densities are analyzed based on the coupling model [29,39]. The FWHM of shock pressure is about 15 ns. (c) Stress-strain relationship of the PDMS film [55]. (d) Launch velocities for different mesh strategies, showing the convergency condition for the LIPIT with and without elastomer.

$$\Pi_v = g\left(\Pi_p, \ \Pi_S, \ \Pi_I, \ \Pi_{M_m}\right). \tag{13}$$

It is obvious that there is a geometrical scaling law for the launch velocity of micro-projectiles in LIPIT.

## 3. Experimental results

In this section, the LIPIT system is established. Based on the experimental method, the launch velocities of the micro-projectiles in the configurations with and without elastomer are measured under various parameter windows, providing experimental data for validating the numerical simulation in Section 4.

As shown in Fig. 1(a), the LIPIT process [49,50] was achieved by a Q-switched Nd: YAG pulsed laser, ultra-high-speed camera with $5 \times 10^6$ fps frame rate, synchronous trigger, an SI-LUX640 visible high power pulsed diode laser illumination source, a convex lens with the focal

length of 60 cm, and a launchpad. The pulsed laser with 1064 nm wavelength has a maximum output energy of 2.5 J and a FWHM of approximately 10 ns [24,51]. The focused spot radius of the laser pulse irradiated on the aluminum film is in the range of 0.3 ∼ 1.7 mm. The adopted energy is between 0.04 ∼ 0.60 J per shot. The launchpad assembly comprises a BK7 glass substrate, a commercial aluminum film (purchased from 3 M company) directly attached to the glass, a PDMS film layer, and a micro-projectile. The PDMS film is directly fabricated on the surface of the aluminum film through the spin-coating method, where the SYLGARD 184 silicone elastomer base with 10 wt.% curing agent cures at 100 °C for 45 mins. The $\Phi 25.4 \times 4$ mm BK7 glass is used as the confined material. The aluminum films with a thickness varying from 30 to 80 μm are used as a laser absorption layer. When the aluminum film is not fully evaporated, it also acts as a confined layer. Two kinds of launchpads are considered. One contains a thin layer of

**Table 2**
Material properties of the aluminum film [54].

| (GPa) | $\nu_m$ | $A_m$ (MPa) | $B_m$ (MPa) | $C_m$ | $n_m$ |
|---|---|---|---|---|---|
| 72 | 0.34 | 200 | 426 | 0.0615 | 0.34 |

**Table 3**
EOS parameters of the aluminum film [54].

| $(kg \cdot m^{-3})$ | $C_{m0}$ $(m \cdot s^{-1})$ | $S_1$ | $S_2$ | $S_3$ | $\gamma_m$ | $a_m$ |
|---|---|---|---|---|---|---|
| 2700 | 5164 | 1.34 | 0 | 0 | 2 | 0.46 |

**Table 4**
Material properties of the PDMS film [55].

| $(kg \cdot m^{-3})$ | $\nu_e$ | $\mu_1$(MPa) | $\alpha_1$ | $\mu_2$(MPa) | $\alpha_2$ |
|---|---|---|---|---|---|
| 1230 | 0.45 | 0.146 | −3.162 | −0.131 | −3.599 |

PDMS film covering the surface of the aluminum film, as shown in Fig. 1 (b1), to attenuate the shock wave and protect the micro-projectile from the laser-induced shock wave, and the other does not use the PDMS film [23] as shown in Fig. 1(b2).

A micro-projectile is placed directly on the aluminum film for the configuration without PDMS film. For the configuration with PDMS film, the PDMS film with a thickness varying from 25 to 100 μm is spin-coated on the aluminum film and then a micro-projectile is placed on the back free surface of the PDMS film. Four kinds of micro-projectiles are used in the LIPIT experiments, i.e. the aluminum micro-projectiles with 20 μm in diameter and 0.0113 μg in weight, the silica micro-projectiles with 50 μm in diameter and 0.173 μg in weight, the silica micro-projectiles with 100 μm in diameter and 1.388 μg in weight, and the steel micro-projectiles with 350 μm in diameter and 175.8 μg in weight.

As the micro-particles with diameters ranging from 20 to 350 μm are very small, the surface adhesive forces of the micro-particles are adequate to attach the micro-particles to the PDMS or aluminum films.

Five LIPIT experiments are carried out for each experimental configuration, i.e. with and without PDMS film, respectively. The details of the experimental parameters are listed in Table 1, where $E_L$ is the energy of a single laser pulse, $R$ is the radius of the laser spot, $E_{Ld}$ is the peak laser power density, $p_0$ is the peak shock pressure calculated from Eqs. (1)-(3) [29,39], $h_{Al}$ is the thickness of the aluminum film, $h_{PDMS}$ is the thickness of the PDMS film, $M_P$ denotes micro-projectile's mass, $v_{P-E}$ represents the experimental launch velocity of the micro-projectile. The launch velocity is the velocity of the micro-projectile at the end of the acceleration stage during experiments. The measurement uncertainty of $v_{P-E}$ is introduced by the imaging system in each experiment.

## 4. Numerical simulation

To validate the scaling law and investigate the influence of the key dimensionless parameters as given by Eqs. (11) and (13), numerical simulation models of the LIPIT with and without elastomer film were built by using LS-DYNA Version 970 [52,53], which is validated by the LIPIT experimental results.

### 4.1. Numerical simulation model

The numerical simulation model of the LIPIT is shown in Fig. 2(a). A 1/4 model is built to increase the computational efficiency due to symmetries of the geometry and the pressure distribution [24]. The symmetrical boundary condition *BOUNDARY_SPC_SET is applied on the lateral surfaces. The laser shock pressure is applied on the top surface of the aluminum film by using *LOAD_SEGMENT_SET. The whole model is meshed with hexahedral Lagrangian elements, and the loading

area is finely meshed to ensure computational accuracy. The spatial and temporal distribution of the shock pressure is given as follows [29,39],

$$p(t,r) = p(t)e^{-\frac{2r^2}{R^2}}, \tag{14}$$

where $p(t)$ represents the temporal distribution of the shock pressure, $r$ denotes the distance from the laser spot center. According to the previous studies [29,39,54], the shock pressure histories on aluminum film at different laser power densities are analyzed as given in Fig. 2(b). At the beginning, the shock pressure increases rapidly to the peak value during laser irradiation, followed by the long-term decay due to the cooling process of the plasma after the laser is switched off. It is worth noting that the shock pressure profiles will change if a different absorption layer is employed due to different laser absorption coefficient and impact impedance of the material.

The Johnson-Cook constitutive model *MAT_JOHSON_COOK [56], as given by Eq. (4), is employed to describe the mechanical behavior of the aluminum film, and the Mie-Grüneisen EOS *EOS_GRUNEISEN as given by Eq. (5) [54] is used to describe its volumetric compressibility. The related parameters of the aluminum film are listed in Tables 2 and 3 [54]. It is to be noted that the Johnson-Cook constitutive model is generally applicable for loading rates up to $10^4$ s$^{-1}$, beyond which the flow stress is underestimated by the Johnson-Cook constitutive model due to the transformation of the deformation mechanism from thermally activated dislocation motion to dislocation drag [57–60]. In the present study, the maximum strain rate near the shock surface of the aluminum film is around $10^5 \sim 10^6$ s$^{-1}$, and it lasts for about 10 ns. With the laser-induced shock wave propagation in the aluminum film, the strain rate decreases quickly below $10^4$ s$^{-1}$. After the stress wave transmits back and forth in the aluminum film several times, the aluminum film expands and accelerates the micro-projectile gradually. As the duration of the launch process of the micro-projectile is more than ten times the initial high loading rate duration, the underestimation of the flow stress in the initial loading duration has a slight influence on the launch velocity of the micro-projectile. As a result, the present numerical model can well predict the launch velocity when compared to the experimental results, indicating that it is reasonable to simulate the LIPIT process with Johnson-Cook constitutive model. In the future, we will try to modify the constitutive model under ultra-high strain rates to improve the simulation model.

The Ogden Rubber constitutive model *MAT_OGDEN_RUBBER [61] is taken to describe the super-elasticity of the PDMS film under impact [45,46]. The related parameters of the PDMS film are fitted according to the measurement results [55] as given in Fig. 2(b) and listed in Table 4, where $\rho_e$ is the density of the PDMS film, $\nu_e$ is the Poisson's ratio of PDMS film. The densities of the aluminum, silica, and steel micro-projectiles are 2700 kg/m$^3$, 2650 kg/m$^3$, and 7830 kg/m$^3$, respectively. The simulation cases without the PDMS film, i.e. cases 1 ∼ 5, are meshed with 55,366 hexahedral Lagrangian elements. The simulation cases with the PDMS film, i.e. case 6 and cases 7 ∼ 10, are meshed with 92,227 and 125,737 hexahedral Lagrangian elements, respectively. The minimum element size of the models is one-fifteenth of the diameter of the micro-projectiles.

### 4.2. Validation of numerical simulation model

Firstly, the mesh sensitivity of the numerical model [62] is performed. Here, cases 4 and 5 for the configuration without PDMS film and cases 8 and 10 for the configuration with PDMS film are investigated for analyzing the convergency of element size, respectively. The simulated launch velocities of the micro-projectiles with different mesh strategies are shown in Fig. 2(d). It is clearly shown that for cases 4 and 5 the simulation results with 55,366 elements and with 108,982 elements are almost identical to each other, and for cases 8 and 10 the launch velocities with 125,737 elements and with 249,724 elements are nearly the same for each other, indicating the convergency of the element size.

**Table 5**
Experimental velocities and numerically predicted velocities of LIPIT.

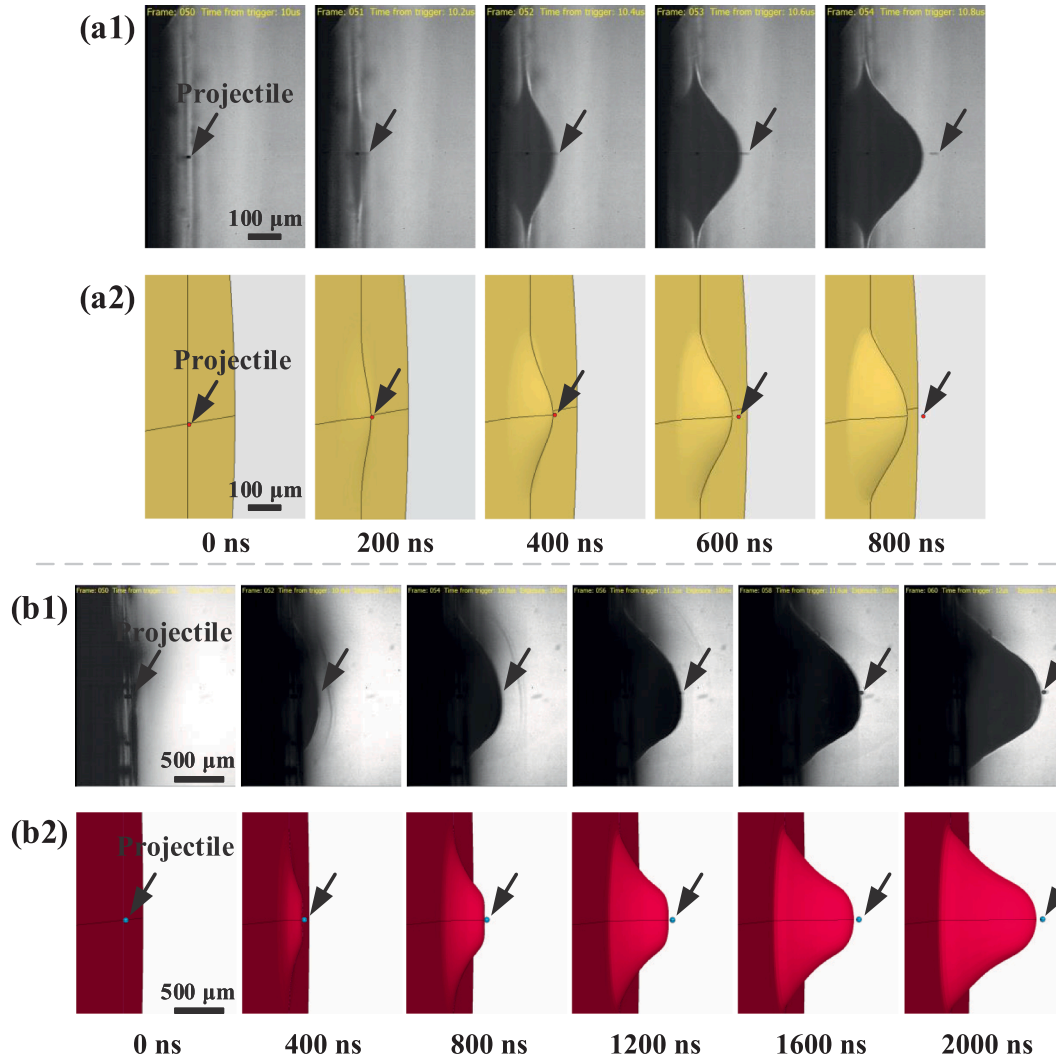| Case | 1 | 2 | 3 | 4 | 5 | 6 | 7 | 8 | 9 | 10 |
|---|---|---|---|---|---|---|---|---|---|---|
| Experiment (m/s) | 364.0 | 473.0 | 331.0 | 129.0 | 118.0 | 511.0 | 157.0 | 234.0 | 73.0 | 81.0 |
| Simulation (m/s) | 360.5 | 445.3 | 372.3 | 153.1 | 122.5 | 474.1 | 182.1 | 249.5 | 81.4 | 88.5 |
| Error (%) | 0.9 | 5.8 | 12.4 | 18.6 | 3.8 | 7.2 | 15.9 | 6.6 | 11.5 | 9.2 |



**Fig. 3.** (a1) Experimental and (a2) simulated launching processes of LIPIT without PDMS film (case 2 in Table 1), and (b1) experimental and (b2) simulated launching processes of LIPIT with PDMS film (case 6 in Table 1). The numerical simulation results agree with the experimental observation, showing the capability of the numerical models for predicting the LIPIT processes.

**Table 6**
Variables for validating the scaling law.

| Parameters | Case 4 | Case 4–1 | Case 4–2 | Case 7 | Case 7–1 | Case 7–2 |
|---|---|---|---|---|---|---|
| $p_0$(GPa) | 0.6200 | 0.3174 | 1.0713 | 1.0600 | 0.5427 | 1.8317 |
| $S_0$ (mm$^2$) | 0.785 | 0.322 | 1.766 | 0.785 | 0.322 | 1.766 |
| $t_0$(ns) | 10.0 | 8.0 | 12.5 | 10.0 | 8.0 | 12.5 |
| $\rho_m$(g/cm$^3$) | 2.70 | 2.16 | 3.24 | 2.70 | 2.16 | 3.24 |
| $E_m$(GPa) | 72.000 | 36.864 | 124.420 | 72.000 | 36.864 | 124.420 |
| $h_m$(μm) | 40.0 | 32.0 | 60.0 | 40.0 | 32.0 | 60.0 |
| $A_m$(MPa) | 200.0 | 102.4 | 345.6 | 200.0 | 102.4 | 345.6 |
| $B_m$(MPa) | 426.00 | 218.11 | 736.13 | 426.00 | 218.11 | 736.13 |
| $C_{m0}$(m/s) | 5164.0 | 4131.1 | 6196.8 | 5164.0 | 4131.1 | 6196.8 |
| $\rho_e$(g/cm$^3$) | \ | \ | \ | 1.230 | 0.984 | 1.476 |
| $E_e$(MPa) | \ | \ | \ | 1.310 | 0.671 | 2.264 |
| $h_e$(μm) | \ | \ | \ | 100.0 | 80.0 | 150.0 |
| $M_P$(μg) | 1.3880 | 0.2910 | 5.6214 | 1.3880 | 0.2910 | 5.6214 |

Therefore, for cases 1 ∼ 5, the models are meshed with 55,366 elements, and for case 6 and cases 7 ∼ 10 the models are meshed with 92,227 and 125,737 elements, respectively.

Table 5 shows the experimentally measured velocities and the numerically simulated velocities of the micro-projectiles for cases 1 ∼ 10 as listed in Table 1. The maximum and average errors of the simulated velocities are 18.6% and 9.2%, respectively, when compared to the experimental results, validating the numerical simulation models. The experimental and simulated launch processes of cases 2 and 6 are depicted in Fig. 3(a) and (b), respectively. It can be seen that the simulated launch process involving the dynamic expansion of the aluminum film and the PDMS film and the detaching time of the micro-projectiles are in agreement with the experimental observation, showing the capability of the numerical models for predicting the LIPIT processes. It is to be noted that for LIPIT with PDMS film as depicted in

**Table 7**

Dimensionless parameters for validating the scaling law.

| Dimensionless quantities | Case 4 | Case 4–1 | Case 4–2 | Case 7 | Case 7–1 | Case 7–2 |
|---|---|---|---|---|---|---|
| $\Pi_v$ | 0.0437 | 0.0446 | 0.0438 | 0.0304 | 0.0293 | 0.0299 |
| $\Pi_p$ | 116.13 | 116.13 | 116.13 | 67.92 | 67.92 | 67.92 |
| $\Pi_{E_m}$ | 116.13 | 116.13 | 116.13 | 67.92 | 67.92 | 67.92 |
| $\Pi_S$ | 0.0451 | 0.0451 | 0.0451 | 0.0451 | 0.0451 | 0.0451 |
| $\Pi_{A_m}$ | 0.00278 | 0.00278 | 0.00278 | 0.00278 | 0.00278 | 0.00278 |
| $\Pi_{B_m}$ | 0.00592 | 0.00592 | 0.00592 | 0.00592 | 0.00592 | 0.00592 |
| $\Pi_I$ | 89.95 | 89.95 | 89.95 | 52.61 | 52.61 | 52.61 |
| $\Pi_{M_m}$ | 0.0167 | 0.0167 | 0.0167 | \ | | |
| $\Pi_\rho$ | \ | \ | \ | 2.195 | 2.195 | 2.195 |
| $\Pi_{E_c}$ | \ | \ | \ | $2.82 \times 10^{-5}$ | $2.82 \times 10^{-5}$ | $2.82 \times 10^{-5}$ |
| $\Pi_h$ | | \ | \ | 0.4 | 0.4 | 0.4 |
| $\Pi_{M_c}$ | \ | \ | \ | 0.01436 | 0.01436 | 0.01436 |
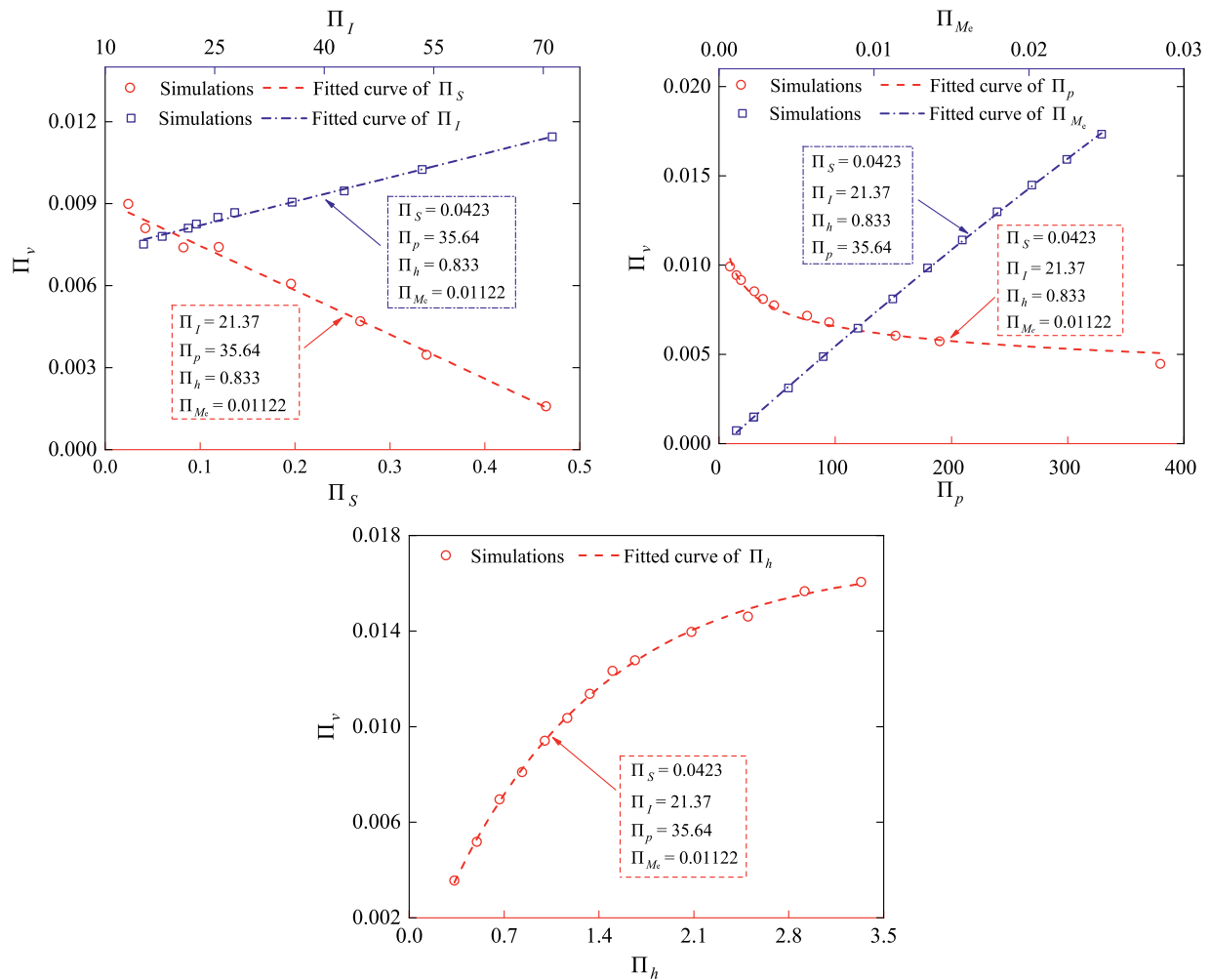


**Fig. 4.** Influences of the dimensionless parameters (a) $\Pi_S$, and $\Pi_I$, (b) $\Pi_p$ and $\Pi_{M_c}$, and (c) $\Pi_h$ on dimensionless launch velocity $\Pi_v$ of micro-projectiles in LIPIT with elastomer film, respectively.

Fig. 3(b), the expanding PDMS film is flattening before 800 ns in numerical simulation. During the acceleration processes of the micro-projectile, a pit of the elastomer will be formed in the contact region with the micro-projectile due to the inertia of the micro-projectile, resulting in the flattening of the elastomer. As it is not obvious in the experiments, the possible reason should be the relatively small elastic modulus of the PDMS film used in numerical simulation when compared to that in experiments, which will be investigated in the future to further improve the computational accuracy of the numerical model. The pit should be more obvious for higher launch velocity, heavier micro-projectile, and softer elastomer. With the continuous expansion of the elastomer, the flattening phenomenon will be disappeared as shown in Fig 3(b).

## 5. Influence of dimensional parameters

Based on the numerical simulations, the scaling laws as described by Eqs. (11) and (13) in Section 2 are firstly validated. The influences of the dimensionless parameters on the dimensionless launch velocity of the micro-projectiles are also analyzed according to the simulation results,
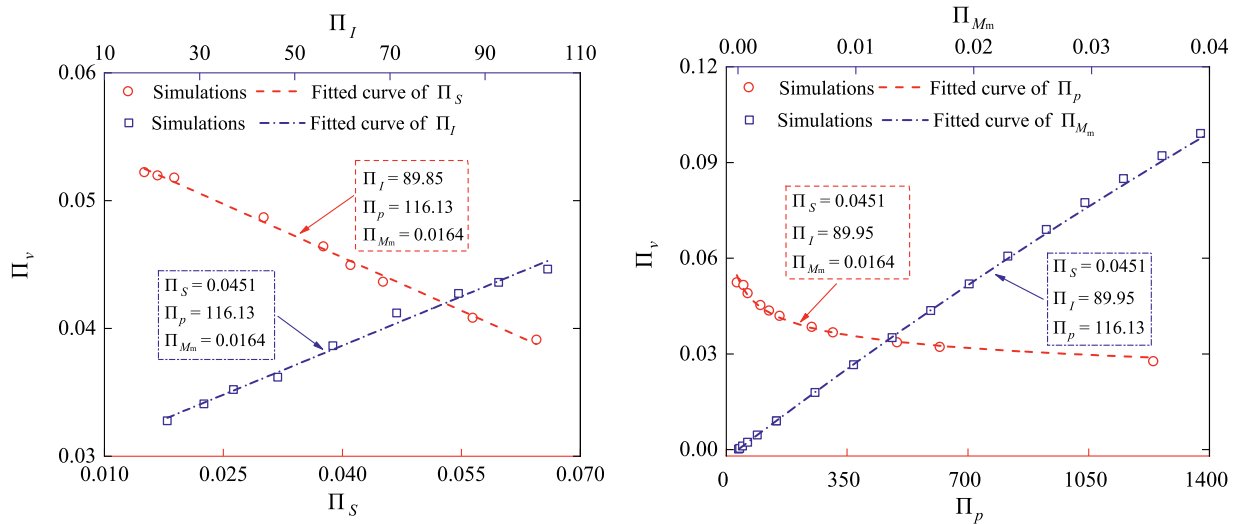
**Fig. 5.** Influences of the dimensionless parameters (a) $\Pi_S$ and $\Pi_I$ and (b) $\Pi_p$ and $\Pi_{M_m}$ on dimensionless launch velocity $\Pi_v$ of micro-projectiles in LIPIT without elastomer film.
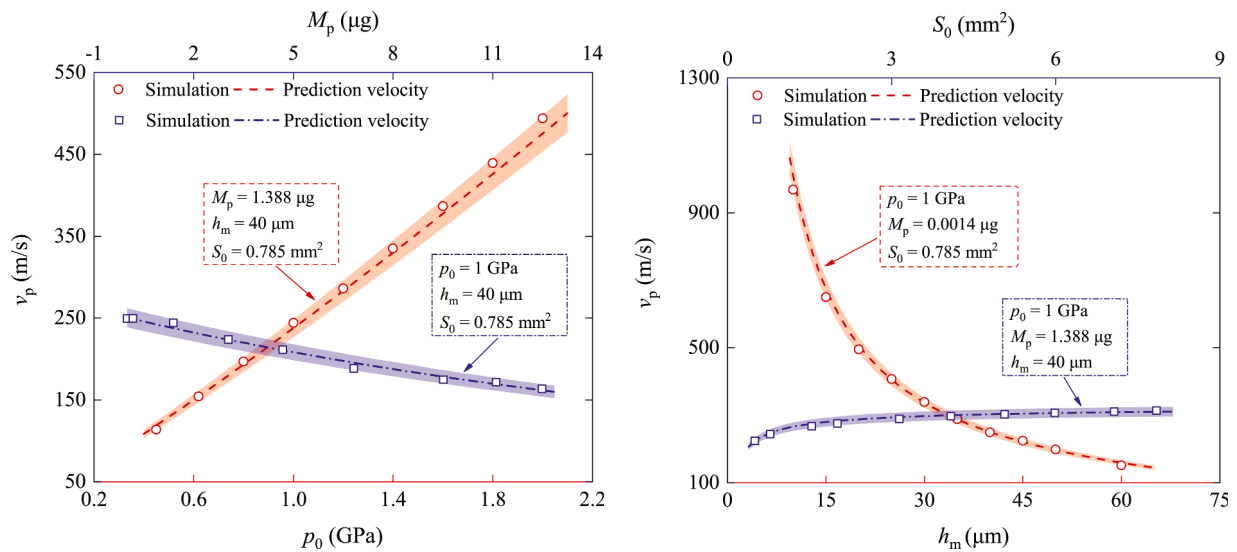


**Fig. 6.** Influences of the parameters (a) $p_0$ and $M_p$, and (b) $h_m$ and $S_0$ on launch velocity $v_p$ of micro-projectiles in LIPIT without elastomer film, showing a good agreement between the numerical simulation results and the predicted results.

**Table 8**
Optimal combination of parameters for the present LIPIT configuration.

| (m/s) | $h_m$ (μm) | $p_0$ (GPa) | $M_p$ (μg) | $S_0$ (mm²) |
|---|---|---|---|---|
| 906.1 | 5 | 0.45 | 0.0014 | 0.785 |
| 968.5 | 10 | 1.00 | 0.0014 | 0.785 |
| 1011.4 | 20 | 2.10 | 0.0014 | 0.785 |
| 934.4 | 30 | 2.95 | 0.0014 | 0.785 |
| 844.6 | 40 | 3.55 | 0.0014 | 0.785 |

from which the specific dimensionless formulas are obtained, providing a method for predicting the launch velocities of micro-projectiles of LIPIT with and without PDMS.

### 5.1. Validation of scaling law

To verify the scaling law as given by Eqs. (10) and (12), the dimensionless parameters are kept constant, but the variables are changed arbitrarily in numerical models. Under this condition, the

dimensionless launch velocity of the micro-projectile is expected to be the same. Therefore, additional cases 4-1, 4-2, 7-1, and 7-2 are simulated, and the related parameters are listed in Tables 6 and 7. Cases 4, 4-1, and 4-2 have different variables but the same dimensionless parameters. Similarly, cases 7, 7-1, and 7-2 have different variables but the same dimensionless parameters. The simulation results of cases 4, 4-1, 4-2, and cases 7, 7-1, 7-2 are also shown in Table 7. The error is in the range of 0.3% ~ 3.7%, validating the scaling law as given by Eqs. (10) and (12).

### 5.2. Influence of dimensional parameters of LIPIT with elastomer film

There are five key dimensionless parameters of the LIPIT with elastomer film, i.e.$\Pi_S$, $\Pi_I$, $\Pi_p$, $\Pi_{M_e}$, and $\Pi_h$. The influence of each dimensionless parameter on the dimensionless launch velocity $\Pi_v$ can be analyzed while keeping the other dimensionless parameters unchanged [63]. Fig. 4(a) shows the simulated influences of $\Pi_S$ and $\Pi_I$ on the dimensionless launch velocity $\Pi_v$. It can be seen that $\Pi_v$ decreases linearly with increasing $\Pi_S$, while it increases linearly with increasing $\Pi_I$.

The influences of $\Pi_S$ and $\Pi_I$ on $\Pi_\nu$ can be described as

$$\Pi_\nu = \left( -1.62 \times 10^{-2} \times \Pi_S + 9.08 \times 10^{-3} \right), \tag{15}$$

$$\Pi_\nu = \left( 6.73 \times 10^{-5} \times \Pi_I + 6.66 \times 10^{-3} \right). \tag{16}$$

Fig. 4(b) shows the influences of $\Pi_p$ and $\Pi_{M_e}$ on $\Pi_\nu$. It can be seen that $\Pi_\nu$ decreases nonlinearly with increasing $\Pi_p$, while it increases nonlinearly with increasing $\Pi_{M_e}$. The following relationships can be fitted according to the simulation results,

$$\Pi_\nu = \left( 0.016 \times \Pi_p^{-0.194} \right), \tag{17}$$

$$\Pi_\nu = \left( -0.107 e^{-\frac{1}{0.136} \Pi_{M_e}} + 0.107 \right). \tag{18}$$

The influence of $\Pi_h$ on $\Pi_\nu$ is given in Fig. 4(c), showing an exponential increase of $\Pi_\nu$ with respect to $\Pi_h$. The relationship between $\Pi_\nu$ and $\Pi_h$ can be described as

$$\Pi_\nu = \left( -0.018 e^{-\frac{1}{1.152} \Pi_h} + 0.017 \right). \tag{19}$$

Assuming that the influence of each dimensionless parameter as given by Eqs. (15)–(19) are independent, and have the product form as follows within a certain parameter range,

$$\Pi_\nu = f_1\left(\Pi_p\right)f_2\left(\Pi_S\right)f_3\left(\Pi_I\right)f_4\left(\Pi_h\right)f_5\left(\Pi_{M_e}\right). \tag{20}$$

According to Eqs. (15)–(20), the following empirical equation can be used to describe the relationship between the dimensionless launch velocity $\nu_p M_p / p_0 S_0 t_0$ and the aforementioned five dimensionless parameters of LIPIT with elastomer film,

$$\Pi_\nu = \alpha \left( -1.62 \times 10^{-2} \times \Pi_S + 9.08 \times 10^{-3} \right)\left( 6.73 \times 10^{-5} \times \Pi_I + 6.66 \times 10^{-3} \right)$$
$$\left( 0.016 \times \Pi_p^{-0.194} \right)\left( -0.107 e^{-\frac{1}{0.136}\Pi_{M_e}} + 0.107 \right)\left( -0.018 e^{-\frac{1}{1.152}\Pi_h} + 0.017 \right), \tag{21}$$

where $\alpha$ is a constant and determined as $\alpha = 2.19 \times 10^8$ with a margin of error of $\pm 0.14 \times 10^8$ by using the data in Fig. 4. According to Eq. (21), the launch velocity of the micro-projectile, $\nu_p$, in case 6 as listed in Table 1, is calculated to be 477.4 m/s. The error of the prediction is 6.57% when compared to the experimental result of 511 m/s, indicating the applicability of Eq. (21) for LIPIT with elastomer film in the present ranges of dimensionless parameters, i.e. $\Pi_S = 0.024 \sim 0.47$, $\Pi_I = 15 \sim 72$, $\Pi_p = 9 \sim 380$, $\Pi_{M_e} = 0.0001 \sim 0.026$, and $\Pi_h = 0.3 \sim 3.5$. Once the dimensionless parameters exceed the ranges, the empirical Eq. (21) should be revisited. From Eq. (21), higher dimensionless launch velocity could be achieved for the LIPIT with elastomer film by increasing the dimensionless parameters $\Pi_I$, $\Pi_{M_e}$, and $\Pi_h$ and decreasing the dimensionless parameters $\Pi_S$ and $\Pi_p$.

### 5.3. Influence of dimensional parameters of LIPIT without elastomer film

Using the same procedure as in Section 5.2, the influences of $\Pi_S$, $\Pi_I$, $\Pi_p$, and $\Pi_{M_m}$ on $\Pi_\nu$ are shown in Fig. 5. Similarly, the following empirical equation can be derived for LIPIT without elastomer film while assuming the influences of these dimensionless parameters are independent,

$$\Pi_\nu = \beta \left( -0.278 \times \Pi_S + 5.67 \times 10^{-2} \right)\left( 1.54 \times 10^{-4} \times \Pi_I + 2.94 \times 10^{-2} \right)$$
$$\left( 9.90 \times 10^{-2} \times \Pi_p^{-0.173} \right)\left( -0.437 e^{-\frac{1}{0.155}\Pi_{M_m}} + 0.437 \right), \tag{22}$$

where $\beta$ is a constant and determined as $\beta = 1.21 \times 10^4$ with a margin of error of $\pm 0.056 \times 10^4$ by using the data in Fig. 5. According to Eq. (22), the launch velocity of the micro-projectile, $\nu_p$, in case 1 as listed in Table 1, is estimated to be 355.3 m/s. The prediction error is 2.39% when compared to the experimental result of 364 m/s, indicating the

applicability of Eq. (22) for LIPIT without elastomer film. From Eq. (22), higher dimensionless launch velocity could be achieved for the LIPIT with elastomer film by increasing the dimensionless parameters $\Pi_I$ and $\Pi_{M_m}$, and by decreasing the dimensionless parameters $\Pi_S$ and $\Pi_p$.

According to Eq. (22), the relationships between the launch velocity $\nu_p$ and the peak pressure $p_0$, the mass of micro-projectile $M_P$, the thickness of the aluminum film $h_e$, and the effective loading area $S_0$ are analyzed for LIPIT without elastomer as shown in Fig. 6, where the shaded areas are the error bars resulting from the fitting error of the parameter $\beta$. The numerical simulation velocity of the micro-projectile is also given, showing a good agreement between the numerical simulation results and the predicted results by empirical Eq. (22). From Fig. 6, higher launch velocity can be achieved by increasing the peak pressure $p_0$ and the effective loading area $S_0$, and by decreasing the mass of micro-projectile $M_p$ and the thickness of the aluminum film $h_e$. For higher shock pressure and thinner aluminum film, the aluminum film might be bursted under shock pressure, which will limit the launch velocity. Taking $S_0 = 0.785$ mm$^2$ (1 mm in diameter) and $M_p = 0.014$ μg (aluminum micro-projectile with 10 μm in diameter), the launch velocity of the micro-projectile under difference $p_0$ and $h_e$ are obtained by numerical simulations, from which the maximum launch velocity is obtained and the optimal combination of $p_0$ and $h_e$ are listed in Table 8. The velocity of the micro-projectile can reach ~1 km/s for the case of $h_e = 20$ μm, $p_0 = 2.10$ GPa, $M_P = 0.0014$ μg, and $S_0 = 0.785$ mm$^2$.

## 6. Conclusions

The paper aimed to develop a method for predicting the launch velocity of micro-projectile in LIPIT experiments. Therefore, the LIPIT experiments, dimensional analysis, and numerical simulation are conducted. The scaling laws with specific dimensionless formulas for LIPIT with and without elastomer film are obtained. The main conclusions can be drawn as follows.

The key parameters that control the launch velocity of the micro-projectile in LIPIT with and without elastomer film are obtained through dimensional analysis. If keeping the materials unchanged, the scaling laws for the LIPIT can be attained. Under this condition, the dimensionless pressure $\Pi_p$, characteristic thicknesses $\Pi_S$ and $\Pi_h$, dimensionless momentum $\Pi_I$, and dimensionless mass $\Pi_{M_e}$ are the five key dimensionless parameters for LIPIT with elastomer film, while the dimensionless pressure $\Pi_p$, characteristic thickness $\Pi_S$, dimensionless momentum $\Pi_I$, and dimensionless mass $\Pi_{M_m}$ are the four key dimensionless key parameters for LIPIT without elastomer film.

To validate the scaling law, the launch process of the LIPIT is investigated by LIPIT experiments and numerical simulations. The launch velocities of the micro-projectiles in the configurations with and without elastomer are measured under various parameter windows using a newly developed LIPIT system. Based on the experimental configuration, the numerical models are built. The results from the numerical modes are in good agreement with that from LIPIT experiments, indicating the capability of the numerical model for capturing the launch mechanism of LIPIT. Based on numerical simulations, the scaling laws of LIPIT are also validated.

The influences of the key dimensionless parameters on the dimensionless launch velocity of micro-projectiles are obtained by using the validated numerical models. The results show that the dimensionless launch velocity of LIPIT with PDMS film increases with increasing the dimensionless parameters $\Pi_I$, $\Pi_{M_e}$, and $\Pi_h$, and with decreasing the dimensionless parameters $\Pi_S$ and $\Pi_p$. For LIPIT without PDMS film, the dimensionless launch velocity increases with increasing the dimensionless parameters $\Pi_I$ and $\Pi_{M_m}$, and with decreasing the dimensionless parameters $\Pi_S$ and $\Pi_p$. According to the simulation results, the empirical dimensionless formulas for LIPIT are obtained, providing a useful method for predicting the launch velocity.

Overall, this paper presents experiments, dimensional analysis, and numerical simulation on the launch processes of LIPIT with and without

elastomer film. The scaling laws of launch velocity of LIPIT with relative thick metallic film are attained and validated for the first time, which can be used to predict the launch velocity of LIPIT. It can also be used to optimize the configuration of LIPIT to achieve high impact velocity.

## CRediT authorship contribution statement

**Z.P. Gu:** Methodology, Investigation, Writing – original draft. **Y.J. Cheng:** Investigation, Formal analysis, Writing – original draft. **K.L. Xiao:** Methodology, Validation. **K. Li:** Writing – review & editing. **X.Q. Wu:** Conceptualization, Writing – review & editing, Supervision, Funding acquisition. **Q.M. Li:** Conceptualization, Writing – review & editing. **C.G. Huang:** Writing – review & editing.

## Declaration of Competing Interest

The authors declare that they have no known competing financial interests or personal relationships that could have appeared to influence the work reported in this paper.

## Acknowledgments

## Appendix

### I. Influence of micro-projectile diameter

In the dimensional analysis and the numerical simulation, the micro-projectile is simplified as a mass point, and therefore, its diameter is not taken into account. Here, the influence of micro-projectile diameter is numerically investigated, as shown in Fig. A1. Under the condition of the same mass, the density of the micro-projectile is changed to realize different diameters of the micro-projectile. It is clearly shown that the launch velocity is almost the same for the micro-projectiles with the same mass but different diameters, indicating that the influence of micro-projectile diameter is negligible within the diameter range in the present study. However, under some extreme conditions, the diameter of the micro-projectile is comparable to the laser spot size, as shown by Veysset et al. [23] and Thevamaran et al. [64], the diameter of the micro-projectile should be taken into account for the derivation of the scaling law.
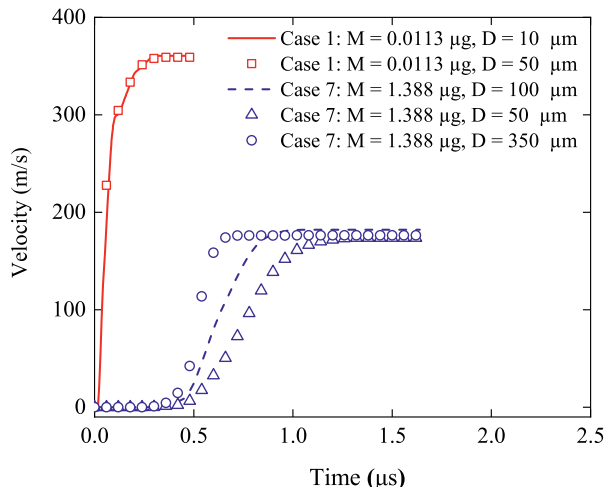


**Fig. A1.** Simulated launch velocities of LIPIT (case 1 and case 7 in Table 1) with the same mass but with different diameters of the micro-projectile.

### II. Influence of deformation of micro-projectile

In the present study, the micro-projectile is assumed as rigid, i.e. the deformation is not considered. If taking the micro-projectile as elasto-plastic material in numerical simulation, the micro-projectile will experience plastic deformation near the aluminum film's contact region, as shown in Fig. A2. However, the launch velocity of the micro-projectile is almost identical to that in the rigid body model. In LIPIT, the deformed region will not contact the tested target. Therefore, the deformation of the micro-projectile will not affect the test results. As a result, the micro-projectile can be regarded as a rigid body in dimensional analysis and numerical simulation to simplify the problem and increase computational efficiency.
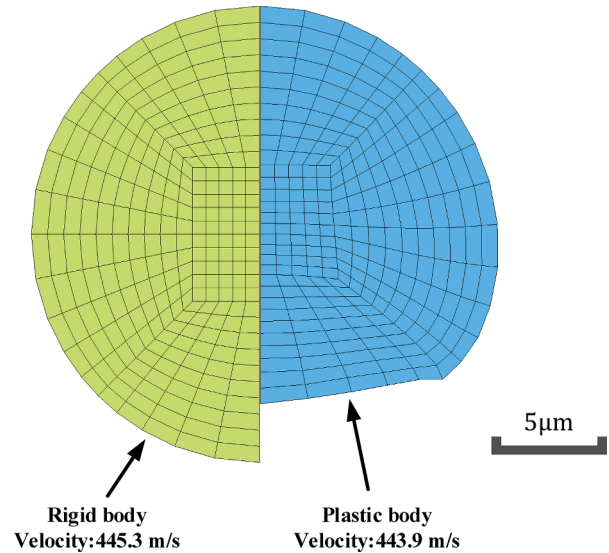


**Fig. A2.** Launch velocities and deformation behavior of micro-projectiles in the rigid model and the deformable model in numerical simulations (case 2 in Table 1).

### III Influence of the thermal softening of the Johnson-Cook constitutive model

In the numerical simulation, the thermal softening effect of the Johnson-Cook constitutive model is not considered. To study the influence of the thermal softening on the numerically simulated launch velocities of micro-projectiles, a numerical simulation (case 2) with the thermal softening effect of the Johnson-Cook constitutive model was performed. The initial temperature is 294.0 K. The melt temperature of the aluminum is 933 K. The thermal softening parameter of the Johnson-Cook constitutive model, $m$, is 1.7 [54]. The simulation results show that during the launch process the average increase of the temperature is about 9.2 K in the loading area of the aluminum film, and the maximum increase of the temperature of the aluminum film located at the contact region with the micro-projectile is about 132 K. The launch velocities of a micro-projectile with and without the thermal softening effect of the Johnson-Cook constitutive model are shown in Fig. A3. The launch velocity of the micro-projectile with the thermal softening effect of the Johnson-Cook constitutive model is 444.3 m/s, and the launch velocity of the micro-projectile without the thermal softening is 445.3 m/s, which is almost identical to that with the consideration of the thermal softening effects. Therefore, to improve the computational efficiency, the Johnson-Cook constitutive model without the thermal softening effect is employed in the present study.
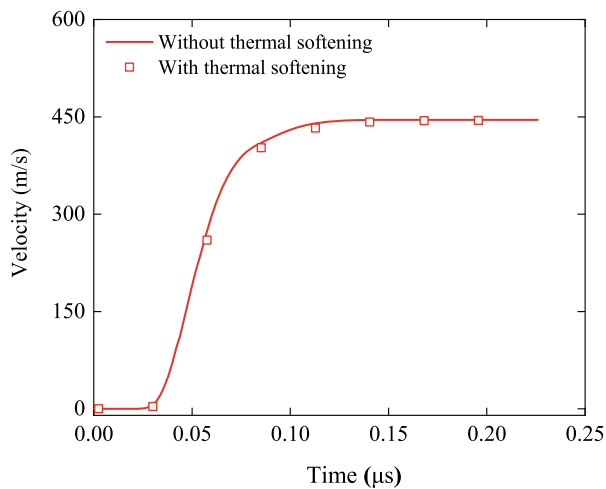
**Fig. A3.** Simulated launch velocities of LIPIT (case 2 in Table 1) with and without thermal softening part of the Johnson-Cook constitutive model.

## References

[1] HassaniGangaraj M, Veysset D, Nelson KA, Schuh CA. *In-situ* observations of single micro-particle impact bonding. Scr Mater 2018;145:9–13.

[2] Lee J, Loya PE, Lou J, Thomas EL. Dynamic mechanical behavior of multilayer graphene via supersonic projectile penetration. Science 2014;346(6213):1092–6.

[3] Kapitaniak M, Vaziri V, Paez Chavez J, Wiercigroch M. Experimental studies of forward and backward whirls of drill-string. Mech Syst Signal Process 2018;100:454–65.

[4] Jaksic N, Foong CH, Wiercigroch M, Boltezar M. Parameter identification of the fatigue-testing rig. Int J Mech Sci 2008;50(7):1142–52.

[5] Foong CH, Wiercigroch M, Deans WF. Novel dynamic fatigue-testing device: design and measurements. Meas Sci Technol 2006;17(8):2218–26.

[6] Wiercigroch M, Kovacs S, Zhong S, Costa D, Vaziri V, Kapitaniak M, Pavlovskaia E. Versatile mass excited impact oscillator. Nonlinear Dynam 2020;99(1):323–39.

[7] Yu R, van Beers L, Spiesz P, Brouwers HJH. Impact resistance of a sustainable Ultra-High Performance Fibre Reinforced Concrete (UHPFRC) under pendulum impact loadings. Constr Build Mater 2016;107:203–15.

[8] Gilbert M, Hobbs B, Molyneaux TCK. The performance of unreinforced masonry walls subjected to low-velocity impacts: experiments. Int J Impact Eng 2002;27(3):231–51.

[9] Liu B, Guedes Soares C. Effect of strain rate on dynamic responses of laterally impacted steel plates. Int J Mech Sci 2019;160:307–17.

[10] Field JE, Walley SM, Proud WG, Goldrein HT, Siviour CR. Review of experimental techniques for high rate deformation and shock studies. Int J Impact Eng 2004;30(7):725–75.

[11] Sulsky D, Schreyer HL. Axisymmetric form of the material point method with applications to upsetting and Taylor impact problems. Comput Method Appl M 1996;139(1–4):409–29.

[12] Lee YS, Wetzel ED, Wagner NJ. The ballistic impact characteristics of Kevlar (R) woven fabrics impregnated with a colloidal shear thickening fluid. J Mater Sci 2003;38(13):2825–33.

[13] Lopatnikov SL, Gama BA, Haque MJ, Krauthauser C, Gillespie JW. High-velocity plate impact of metal foams. Int J Impact Eng 2004;30(4):421–45.

[14] Veysset D, Lee JH, Hassani M, Kooi SE, Thomas EL, Nelson KA. High-velocity micro-projectile impact testing. Appl Phys Rev 2021;8(1):011319.

[15] Hyon J, Lawal O, Fried O, Thevamaran R, Yazdi S, Zhou M, Veysset D, Kooi SE, Jiao Y, Hsiao M-S, Streit J, Vaia RA, Thomas EL. Extreme energy absorption in glassy polymer thin films by supersonic micro-projectile impact. Mater Today 2018;21(8):817–24.

[16] Veysset D, Sun Y, Lem J, Kooi SE, Maznev AA, Cole ST, Mrozek RA, Lenhart JL, Nelson KA. High-strain-rate behavior of a viscoelastic gel under high-velocity microparticle impact. Exm Mech 2020;60(9):1179–86.

[17] Hyon J, Lawal O, Thevamaran R, Song YE, Thomas EL. Extreme energy dissipation via material evolution in carbon nanotube mats. Adv Sci 2021;8(6):2003142.

[18] Portela CM, Edwards BW, Veysset D, Sun Y, Nelson KA, Kochmann DM, Greer JR. Supersonic impact resilience of nanoarchitected carbon. Nat Mater 2021;20:1491–7.

[19] Chen SH, Souna AJ, Soles CL, Stranick SJ, Chan EP. Using microprojectiles to study the ballistic limit of polymer thin films. Soft Matter 2020;16(16):3886–90.

[20] Xie W, Zhang R, Headrick RJ, Taylor LW, Kooi S, Pasquali M, Muftu S, Lee JH. Dynamic strengthening of carbon nanotube fibers under extreme mechanical impulses. Nano Lett 2019;19(6):3519–26.

[21] Hassani-Gangaraj M, Veysset D, Champagne VK, Nelson KA, Schuh CA. Adiabatic shear instability is not necessary for adhesion in cold spray. Acta Mater 2018;158:430–9.

[22] Lee J, Veysset D, Singer JP, Retsch M, Saini G, Pezeril T, Nelson KA, Thomas EL. High strain rate deformation of layered nanocomposites. Nat Commun 2012;3:1164.

[23] Veysset D, Sun Y, Kooi SE, Lem J, Nelson KA. Laser-driven high-velocity microparticle launcher in atmosphere and under vacuum. Int J Impact Eng 2020;137:103465.

[24] Xiao K, Wu X, Song X, Yuan J, Bai W, Wu C, Huang C. Study on performance degradation and damage modes of thin-film photovoltaic cell subjected to particle impact. Sci Rep UK 2021;11(1):782.

[25] Veysset D, Hsieh AJ, Kooi S, Maznev AA, Masser KA, Nelson KA. Dynamics of supersonic microparticle impact on elastomers revealed by real-time multi-frame imaging. Sci Rep UK 2016;6:25577.

[26] Xiao K, Lei X, Chen Y, An Q, Hu D, Wang C, Wu X, Huang C. Extraordinary impact resistance of carbon nanotube film with crosslinks under micro-ballistic impact. Carbon 2021;175:478–89.

[27] Cai J, Thevamaran R. Superior energy dissipation by ultrathin semicrystalline polymer films under supersonic microprojectile impacts. Nano Lett 2020;20(8):5632–8.

[28] Sun Y, Veysset D, Nelson KA, Schuh CA. The transition from rebound to bonding in high-velocity metallic microparticle impacts: jetting-associated power-law divergence. J Appl Mech T Asme 2020;87(9):091002.

[29] Wu X, Tan Q, Huang C. Geometrical scaling law for laser shock processing. J Appl Phys 2013;114(4):043105.

[30] Zhang WW, Yao YL. Micro scale laser shock processing of metallic components. J Manuf Sci E T ASME 2002;124(2):369–78.

[31] Montross CS, Wei T, Ye L, Clark G, Mai YW. Laser shock processing and its effects on microstructure and properties of metal alloys: a review. Int J Fatigue 2002;24(10):1021–36.

[32] HassaniGangaraj M, Veysset D, Nelson KA, Schuh CA. Melt-driven erosion in microparticle impact. Nat Commun 2018;9:5077.

[33] Brown KE, Shaw WL, Zheng X, Dlott DD. Simplified laser-driven flyer plates for shock compression science. Rev Sci Instrum 2012;83(10):103901.

[34] Wang L, Yan Y, Ji X, Zhang W, Jiang H, Qin W, Wang Y, Tang D. Improving the energy conversion efficiency of a laser-driven flyer by an *in situ*-fabricated nano-absorption layer. Nanoscale Res Lett 2020;15(1):125.

[35] Sun Y, Veysset D, Kooi SE, Nelson KA, Schuh CA. *In situ* observations of jetting in the divergent rebound regime for high-velocity metallic microparticle impact. Appl Phys Lett 2020;117(13):134105.

[36] Hassani M, Veysset D, Sun Y, Nelson KA, Schuh CA. Microparticle impact-bonding modes for mismatched metals: from co-deformation to splatting and penetration. Acta Mater 2020;199:480–94.

[37] Veysset D, Kooi SE, Maznev AA, Tang S, Mijailovic AS, Yang YJ, et al. High-velocity micro-particle impact on gelatin and synthetic hydrogel. J Mech Behav Biomed Mater 2018;86:71–6.

[38] Lienhard J, Veysset D, Nelson KA, Schuh CA. Melting and ejecta produced by high velocity microparticle impacts of steel on tin. J Appl Mech T Asme 2021;88(11):111005.

[39] Wu X, Huang C, Wang X, Song H. A new effective method to estimate the effect of laser shock peening. Int J Impact Eng 2011;38(5):322–9.

[40] Qian Y, Huang H, Wang C, Yu P, Xu J, Zhang Z. Formation of leaf-shaped microstructure on Zr-based metallic glass via nanosecond pulsed laser irradiation. J Manuf Process 2021;72:61–70.

[41] Jiang MQ, Wei YP, Wilde G, Dai LH. Explosive boiling of a metallic glass superheated by nanosecond pulse laser ablation. Appl Phys Lett 2015;106(2):021904.

[42] Jiang MQ, Wu XQ, Wei YP, Wilde G, Dai LH. Cavitation bubble dynamics during pulsed laser ablation of a metallic glass in water. Extreme Mech Lett 2017;11:24–9.

[43] Gu ZP, Wu XQ, Li QM, Yin QY, Huang CG. Dynamic compressive behaviour of sandwich panels with lattice truss core filled by shear thickening fluid. Int J Impact Eng 2020;143:103616.

[44] Panciroli R, Abrate S, Minak G, Zucchelli A. Hydroelasticity in water-entry problems: comparison between experimental and SPH results. Compose Struct 2012;94(2):532–9.

[45] Khodadadi A, Liaghat G, Shahgholian-Ghahfarokhi D, Chizari M, Wang B. Numerical and experimental investigation of impact on bilayer aluminum-rubber composite plate. Thin Wall Struct 2020;149:106673.

[46] Karagiozova D, Mines RAW. Impact of aircraft rubber tyre fragments on aluminium alloy plates: II - numerical simulation using LS-DYNA. Int J Impact Eng 2007;34(4):647–67.

[47] Buckingham E. On physically similar systems, illustrations of the use of dimensional equations. Phys Rev 1914;4(4):345–76.

[48] Hua S, Chang C, Liu H, Meng F. Numerical and dimensional analysis for the jet buckling of highly viscous fluid. Int J Mech Sci 2021;210:106742.

[49] Sun Y, Wu YCM, Veysset D, Kooi SE, Hu W, Swager TM, Nelson KA, Hsieh AJ. Molecular dependencies of dynamic stiffening and strengthening through high strain rate microparticle impact of polyurethane and polyurea elastomers. Appl Phys Lett 2019;115(9):093701.

[50] Sun Y, Kooi SE, Nelson KA, Hsieh AJ, Veysset D. Impact-induced glass-to-rubber transition of polyurea under high-velocity temperature-controlled microparticle impact. Appl Phys Lett 2020;117(2):021905.

[51] Moosmuller H, She CY. Equal intensity and phase contours in focused Gaussian laser beams. IEEE J Quantum Elect 1991;27(4):869–74.

[52] Zhang B, Zhang X, Wu S, Zhang H. Indentation of expanded polystyrene foams with a ball. Int J Mech Sci 2019;161:105030.

[53] Fernando PLN, Mohotti D, Remennikov A. Behaviour of explosively welded impedance-graded multi-metal composite plates under near-field blast loads. Int J Mech Sci 2019;163:105124.

[54] Wu X, Duan Z, Song H, Wei Y, Wang X, Huang C. Shock pressure induced by glass-confined laser shock peening: experiments, modeling and simulation. J Appl Phys 2011;110(5):053112.

[55] Kim TK, Kim JK, Jeong OC. Measurement of nonlinear mechanical properties of PDMS elastomer. Microelectron Eng 2011;88(8):1982–5.

[56] Weng J, Zhuang K, Hu C, Ding H. A PSO-based semi-analytical force prediction model for chamfered carbide tools considering different material flow state caused by edge geometry. Int J Mech Sci 2020;169:105329.

[57] Hassani M, Veysset D, Nelson KA, Schuh CA. Material hardness at strain rates beyond 10(6) s(-1) via high velocity microparticle impact indentation. Scr Mater 2020;177:198–202.

[58] Armstrong RW, Walley SM. High strain rate properties of metals and alloys. Int Mater Rev 2008;53(3):105–28.

[59] Wang Q, Ma N, Takahashi M, Luo X, Li C. Development of a material model for predicting extreme deformation and grain refinement during cold spraying. Acta Mater 2020;199:326–39.

[60] Lemiale V, King PC, Rudman M, Prakash M, Cleary PW, Jahedi MZ, Gulizia S. Temperature and strain rate effects in cold spray investigated by smoothed particle hydrodynamics. Surf Coat Technol 2014;254:121–30.

[61] Fazekas B, Goda TJ. Closed-form and numerical stress solution-based parameter identification for incompressible hyper-viscoelastic solids subjected to various loading modes. Int J Mech Sci 2019;151:650–60.

[62] Giglio M, Manes A, Vigano F. Ductile fracture locus of Ti-6Al-4V titanium alloy. Int J Mech Sci 2012;54(1):121–35.

[63] Wu X, Wang X, Wei Y, Song H, Huang C. Parametric study on single shot peening by dimensional analysis method incorporated with finite element method. Acta Mech Sinica PRC 2012;28(3):825–37.

[64] Thevamaran R, Lawal O, Yazdi S, Jeon SJ, Lee JH, EL Thomas. Dynamic creation and evolution of gradient nanostructure in single-crystal metallic microcubes. Science 2016;354(6310):312–6.